Eruption style and crystal size distributions: Crystallization of groundmass nanolites in the 2011 Shinmoedake eruption ⚓

MAYUMI MUJIN[1,*], MICHIHIKO NAKAMURA[1], AND AKIRA MIYAKE[2]

[1]Department of Earth Science, Graduate School of Science, Tohoku University, 6-3, Aramaki-Aza-Aoba, Aobaku, Sendai 980-8578, Japan
[2]Department of Geology and Mineralogy, Graduate School of Science, Kyoto University, Kitashirakawaoiwake-cho, Sakyo-ku, Kyoto 606-8502, Japan

ABSTRACT

Crystallization of groundmass minerals may record the physicochemical conditions of magmatic processes upon eruption and is thus a topic of interdisciplinary research in the disciplines of mineralogy, petrology, and volcanology. Recent studies have reported that the groundmass crystals of some volcanic rocks exhibit a break in their crystal size distribution (CSD) slopes that range from a few micrometers to hundreds of nanometers. The crystals consisting of the finer parts of the break were defined as nanolites. In this study, we report the presence of nanometer-scale crystals down to 1 nm in the pyroclasts of the 2011 eruption of Shinmoedake, the Kirishima volcano group, based on field emission-scanning electron microscopy (FE-SEM) and transmission electron microscopy (TEM).

We discovered a gap (hiatus) from ~100 to ~30 nm in the size distribution of pyroxene in a dense juvenile fragment of a vulcanian explosion. The pyroxene crystals ~20–30 nm on a diameter were ferroaugite ($C2/c$), while those a few hundred nanometers in width had a composite structure consisting of the domains of orthopyroxene ($Pbca$), augite ($C2/c$), and sub-calcic augite ($C2/c$). In high-angle annular dark-field scanning TEM images of the same sample, bright spots ~1–2 nm in diameter were recognized with a gap in size from ~10–20 nm titanomagnetite ($Fd\bar{3}m$). They are presumed to have Fe-rich compositions, although their phases were too small to be determined. In addition, we found that crystals smaller than a few tens of nanometers for pyroxene and 100 nm for plagioclase did not exist or their number densities were too low for accurate determination. This indicates that there are practical minimum sizes of the crystals. These observations show that nucleation of the nanoscale crystals almost paused (froze) in the late stage of groundmass crystallization, possibly due to a decrease in undercooling, increase in interfacial free energy, and decrease in diffusivity in a dehydrated melt, whereas crystal growth was mostly continuous. In this paper, we introduce the novel term "ultrananolite," to refer to crystals smaller than 30 nm in diameter, and redefine "nanolite" simply as those 30 nm to 1 μm in width, complementing the size interval of crystals in volcanic groundmass smaller than microlites (1–30 μm). In the transient nucleation process, the presence of subcritical size clusters is required. The observed ultrananolite-sized particles might partly include subcritical clusters. The difference in the slope of CSDs, presence of gaps in size distribution, and minimum crystal size among the eruption styles of the 2011 Shinmoedake eruption may be interpreted by considering the difference in magma residence time and fragmentation pressure in the shallow conduit, and possibly the rewelding process in the crater.

Keywords: Microlite, nanolite, ultrananolite, crystal size distribution, transient nucleation, vulcanian explosion; Rates and Depths of Magma Ascent on Earth

INTRODUCTION

Although nanoscale crystals present in the groundmass of volcanic rocks have long been recognized as "cryptocrystals" (e.g., Johannsen 1931), their mineralogical characteristics have been poorly described. Limited petrological studies on nanoscale crystals include those on the origin of the brownish color (Schlinger et al. 1986; Paulick and Franz 1997) and remnant magnetism (Schlinger et al. 1988) of volcanic glasses that contain nanoscale crystals of Fe-oxide. Sharp et al. (1996) obtained the crystal size distribution (CSD) of pyroxene in the groundmass of the Ben Lomond rhyolite lava dome down to a scale of 100 nm and found a pronounced break of the CSD at 600 nm in width. They termed the smaller group of crystals "nanolites" and reported a core-rim structure showing pigeonite and augite overgrowths on hypersthene.

Because nanolites crystallize at low pressure, they can elucidate near-surface eruption dynamics. Mujin and Nakamura (2014) first reported the presence of groundmass nanolites in quenched pyroclasts from the 2011 eruption of Shinmoedake, the Kirishima volcano group. They proposed that the nanolites recorded the physicochemical conditions of magma at the point of the transition in eruption style. However, nanolites in the 2011 Shinmoedake eruption products have not been fully characterized

in terms of crystallographic phases and solid solution composition; such parameters are essential for further clarifying their crystallization conditions. In this study, we investigated in detail the 2011 Shinmoedake eruption products examined by Mujin and Nakamura (2014). We discovered finer sized crystals of pyroxene (~20–30 nm) and most likely Fe-Ti oxide or amorphous cluster (~1–2 nm) with a clear size gap (hiatus) in a dense juvenile fragment of the vulcanian explosion. We introduce the term "ultrananolite" to refer to crystals smaller than 30 nm in diameter. We redefine "nanolite" alternatively as crystals 30 nm to 1 μm in width. We obtained the chemical compositions and crystal space groups of pyroxene nanolites ~1 μm in width and those of pyroxene and Fe-Ti oxide ~20–30 and ~10–20 nm on a diameter, respectively. The areal number density measurements of pyroxene and Fe-Ti oxide were extended to 1 nm. We then discuss the crystallization processes of nanolite and ultrananolite in terms of nucleation mechanism and phase diagrams. Finally, their implications for the shallow magma ascent processes of the 2011 Shinmoedake eruption are discussed.

OUTLINE OF THE 2011 SHINMOEDAKE ERUPTION

The Shinmoedake volcano is part of the Kirishima volcano group located in southern Kyushu, Japan (Figs. 1a and 1b). The main phase of eruption activity in 2011 is characterized by sub-Plinian eruptions and subsequent lava extrusion with intermittent vulcanian explosions from January 26 to 31 followed by frequent vulcanian explosions from February 1 to March 13 (Miyabuchi et al. 2013; Kozono et al. 2013). This eruption sequence is well documented by various geophysical observations. In the Appendix[1], we present a brief review of geophysical constraints on the magma ascent processes in the 2011 eruption of the Shinmoedake. In the evening of January 26 and the morning and evening of January 27, three major sub-Plinian eruptions were detected by weather radar eruption cloud echo measurements (Shimbori et al. 2013). Geodetic and synthetic aperture radar satellite (SAR) observation revealed that the sub-Plinian eruptions continued for 2.5, 2.5, and 1.75 h, respectively (Kozono et al. 2013). From January 29 to 31, continuous growth of a pancake-shaped mass of lava inside the summit crater was detected by SAR imaging analysis (Ozawa and Kozono 2013). In addition, 13 infrasound-generating vulcanian explosions were reported from 15:41 JST (Japan Standard Time, UTC + 09:00) on January 27 to 19:23 on March 1 (Japan Meteorological Agency 2012).

SAMPLE COLLECTION AND BASIC PETROGRAPHY

In this study, two dense juvenile fragments were examined by scanning electron microscopy (SEM) in addition to the samples examined by Mujin and Nakamura (2014); these rocks include six sub-Plinian pumice clasts, five vulcanian pumice clasts, and three dense juvenile fragments. These samples were collected on July 24, 2011, at Takachihogawara, 3.0 km south of the Shinmoedake crater. Brown, gray, and white colored pumice clasts were collected from a section of well-preserved sub-Plinian fall deposit. The sub-Plinian pumices used in this study were collected from a well-sorted pumice fall deposit (layers 2–5 of Nakada et al. 2013). The fine ash of the January 27, 15 h 41 min vulcanian explosion (unit 3L of Miyabuchi et al. 2013) was excluded. The vulcanian products were collected from the topmost surface of the pumice deposits of the three sub-Plinian eruption columns (layer 5 of
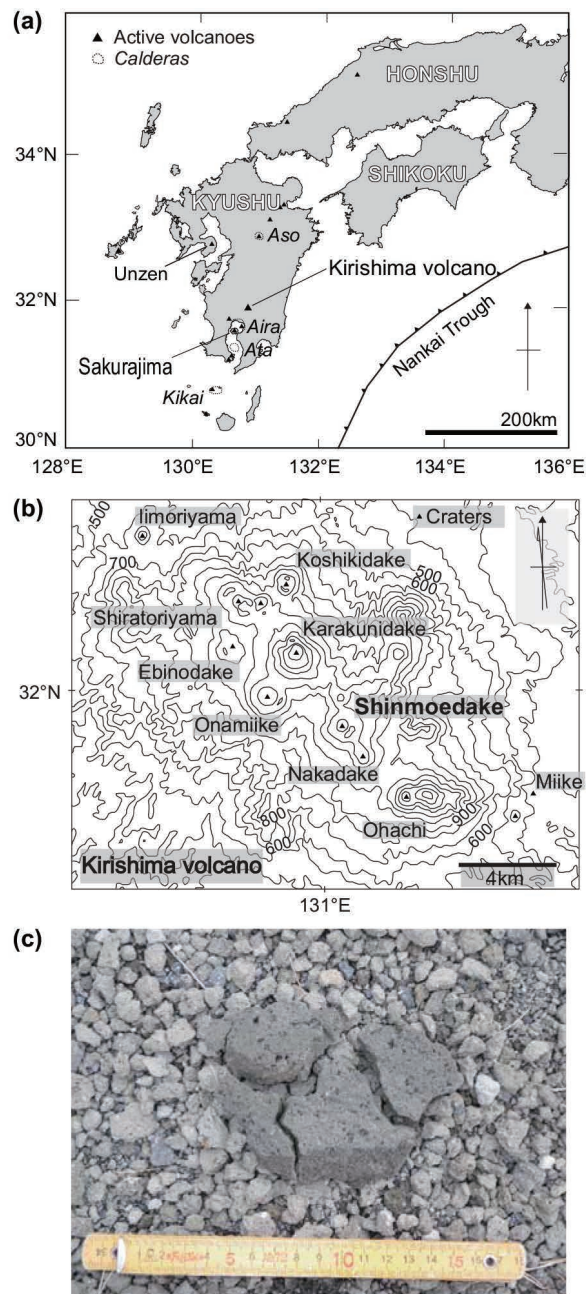

FIGURE 1. (**a**) Location and (**b**) contour maps of the Kirishima volcano group. The coastlines and counters were drawn by MapMap software (vers.6.0; Kamada 2014) and GSI Maps of the Geospatial Information Authority of Japan (2014), respectively. The active volcano and caldera information in this region was obtained from the National Catalog of the Active Volcanoes in Japan (Japan Meteorological Agency 2016), and location of the Nankai trough was obtained from a bathymetric chart of the Japan Coast Guard (JCG 2014). The craters of the Kirishima volcano group were determined from GeomapNavi (2016), a geological map display system of Geological Survey of Japan, National Institute of Advanced Industrial Science and Technology. (**c**) Top surface of the sampling location (Takachihogawara). The well-preserved nature of original deposition was confirmed by jigsaw impact cracks. The scale is in centimeters.

Nakada et al. 2013; unit 3U of Miyabuchi et al. 2013), which consist of glassy, dense juvenile (co-magmatic) fragments of lava and gray-brown pumices that are clearly coarser than the pumices of the sub-Plinian eruption deposit. The well-preserved nature of the original deposition was confirmed by their jigsaw impact cracks (Fig. 1c). The explosion date of the vulcanian sample has not been determined; however, the wind direction and the eruption cloud height reported in the Volcanic Activity Documents by the Japan Meteorological Agency (JMA 2011) indicate likely dates of February 1, February 11, and March 13, 2011. We also collected a chip of glossy volcanic breccia (projectiles) tens of centimeters on a side that formed impact craters on the surfaces of fallout pumice deposits at Nakadake summit, 1.1 km south of the Shinmoedake crater, on July 23, 2015. Suzuki et al. (2013) reported that the gray and brown pumices and dense juvenile fragments are similar in bulk chemical composition (SiO_2 = 57–58 wt%), whereas the white pumice (SiO_2 = 62–63 wt%) is a dacitic end-member of the mixed magma that formed the majority of the 2011 andesite.

The interstitial glass in the groundmass was almost colorless in the sub-Plinian and vulcanian pumices and light brown–brown in a dense fragment. However, the bulk groundmass compositions including groundmass minerals were almost the same for the pumices from the sub-Plinian eruption and pumices and dense juvenile fragments of the vulcanian explosions, at SiO_2 = 63–64 wt% (Mujin and Nakamura 2014). The petrographic features of the volcanic breccias from the Nakadake summit were similar to those of the dense juvenile fragments collected at the Takachihogawara. Low (×5000) and high (×10 000–40 000) magnification backscattered electron (BSE) images of the three types of samples are shown in Figure 2. The principle petrographic features of these samples were reported by Mujin and Nakamura (2014). The modal compositions of plagioclase microlite and nanolite in the groundmass of the three erupted materials are similar at 20–26 area%. The modal compositions of pyroxene microlite and nanolite are 9–13 area%. Using these values and bulk-rock manometric analyses of water content, the water contents in the interstitial glasses of the sub-Plinian pumices, vulcanian pumices, and dense fragments were recalculated to be 0.35, 0.47, and 0.44 wt%, respectively (Mujin and Nakamura 2014).

ANALYTICAL PROCEDURES

FE-SEM-EDS analyses

For SEM analysis, the cut surfaces of samples were polished using alumina powder with a grain size of 0.3–1.0 μm. The flaws and damages caused by mechanical polishing were removed by an Ar-ion milling apparatus (Model 691, GATAN PIPS), with an acceleration voltage of 5 keV at an incident angle of 3° for 10 min, to obtain clear SEM images at a magnification of >×10 000. We obtained digital BSE images of the polished sections at Tohoku University by using an SEM instrument with tungsten filament (W-SEM; S-3400N, Hitachi High-Technologies) at an acceleration voltage of 15 keV. In addition, we used in-lens type high-resolution field emission (FE)-SEM instruments, Hitachi High-Technologies S-5500 and SU9000 at Tohoku University and Hitachi High-Tech Tokyo Solution Lab, respectively, at acceleration voltages of 2–15 keV. For the higher magnification observations with FE-SEM, we applied lower acceleration voltages.

TEM observation

For TEM analyses of a dense juvenile fragment, an ultrathin section was extracted from a slab using a focused ion beam (FIB) system (Quanta 200 3DS, FEI)

at Kyoto University and was observed under a transmission electron microscope (TEM; JEOL JEM-2100F) equipped with CCD cameras (Gatan Orius 200D and 1000D) and an energy-dispersive X-ray spectrometry (EDS; JEOL Silicon Drift Detector) system at Kyoto University. In the FIB system, a Ga⁺ ion gun was used at an acceleration voltage of 30 kV and a beam current of 0.1–30 nA; a beam current of 48 pA at 5 kV was used for the final processing. We conducted TEM observations and EDS analyses at an acceleration voltage of 200 kV. For quantitative X-ray analysis of thin specimens in scanning TEM (STEM), the ζ-factor method (Watanabe and Williams 2006) was applied. Prior to the quantification, the ζ factors were determined for this particular instrument by using a NIST standard reference material 2063a glass thin-film (Reed 1993) as described in Watanabe and Williams (2006). For accurate electron beam current measurements required for the ζ-factor method, one of the CCD cameras was used with appropriate calibration beforehand. The concentration of oxygen in atomic percent was quantified independently. The weight percent of the oxides was calculated from the atomic percent of cations and the molecular weight of oxides. The mineral phases were identified through space group determination with diffraction analyses and by quantitative analyses of chemical compositions. The raw EDS counts of pyroxene, ~20–30 nm on a diameter, were rich in silicon and oxygen compared with the stoichiometric composition owing to the effect of the surrounding glass. To obtain the solid solution compositions, we therefore subtracted the glass composition from the raw data to fit the pyroxene stoichiometry. We used the most differentiated glass composition obtained by spot analyses with W-SEM-EDS in the calculation. Because the concentrations of MgO, FeO, and CaO in the glass were low, the overlapping effect on the solid solution composition was not significant.

SEMI-LOG CSD PLOTS

The semi-log CSD plots of groundmass plagioclase and pyroxene, after stereological corrections with CSDCorrections (Higgins 2000), are shown in Figure 3. The raw data are the same as those in Mujin and Nakamura (2014), and the difference in the plotting procedure from that in Mujin and Nakamura (2014) is presented in the Appendix[1]. The used data are crystals from 0.1 to 5.2 μm in width before CSDCorrections is applied. We traced the crystals in the images manually and counted number of the crystals because the crystals have compositional zoning and small contrast with surrounding glass. The method for discrimination between glass and crystals is presented in Mujin and Nakamura (2014). In Figure 3, the 3D shape of crystals was estimated from the 2D size measurements with CSDSlice (Morgan and Jerram 2006) to correct the effects of intersection probability and cut-sectioning (Table 1). The estimated aspect ratios of the crystal shape converged to a narrow range for the same mineral, although not perfectly (Table 1). We used the aspect ratio and number of bin/decade obtained from the ×5000 images of sub-Plinian pumices, i.e., 1:1:8 and 5, respectively, for pyroxene, and 1:5:10 and 5 for plagioclase. By using a common parameter, we were able to load two separate data sets obtained in different magnifications with W-SEM and FE-SEM to CSDCorrections and produce a single line. The general characteristics of CSDs do not change significantly even if we use different aspect ratios and bin/decade numbers that best fit each data set. The difference in the maximum crystals width between plagioclase and pyroxene (Fig. 3) resulted from the difference in their crystal shapes. Detailed correction conditions are described in the Appendix[1].

All the CSD plots showed a concave upward curvature (Fig. 3). It is known that high-level stereological corrections, including CSDCorrections, may result in excess correction of the number of small crystals (Castro et al. 2003). It should be noted, however, that only the CSD slope of plagioclase in sub-Plinian pumices did not increase with a decrease in size, as pointed out by Mujin and Nakamura (2014) (also see Supplemental[1] Fig. S2).
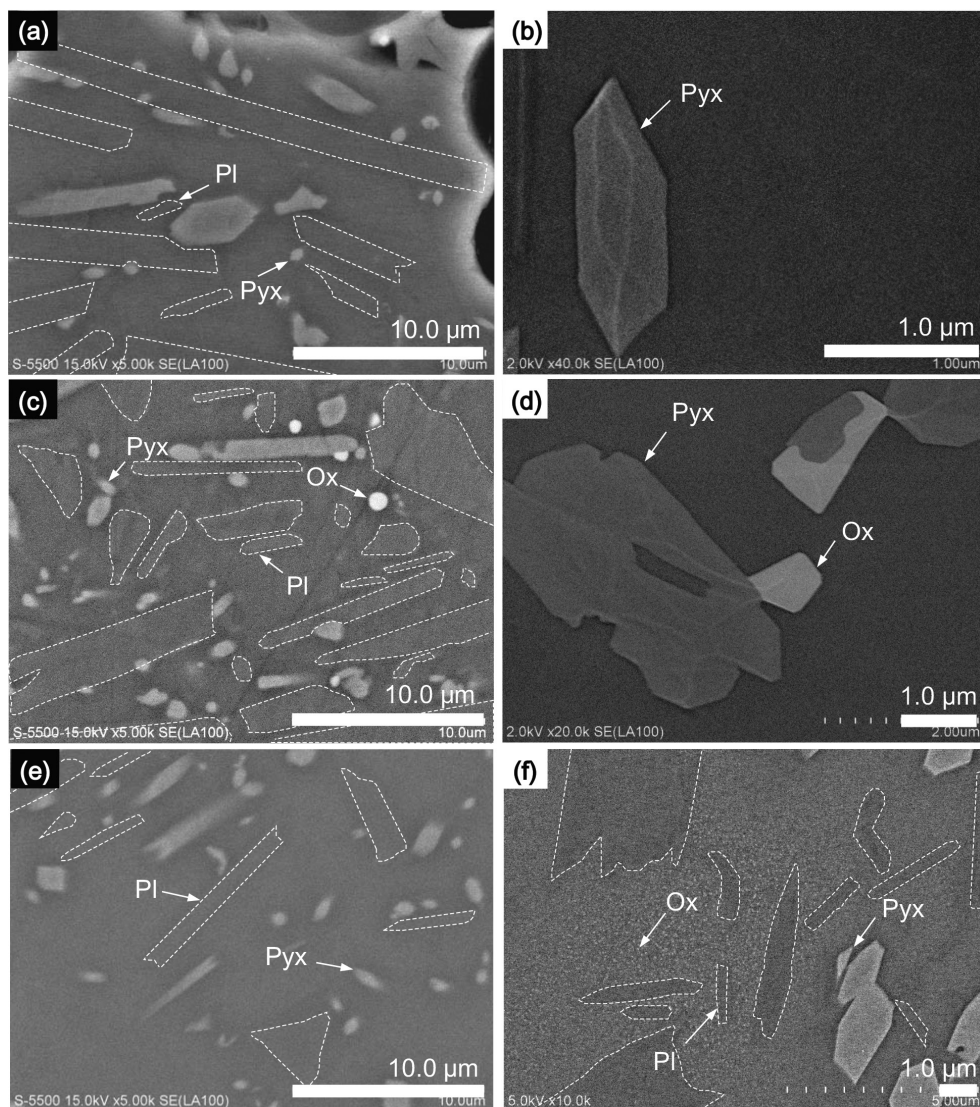
FIGURE 2. Backscattered electron (BSE) images of groundmass of the pyroclasts from the Shinmoedake 2011 eruption. (**a** and **b**) Gray pumice of the sub-Plinian eruption; (**c** and **d**) gray pumice of the vulcanian explosion; and (**e** and **f**) dense juvenile fragment from the vulcanian explosions. Abbreviations: Pl = plagioclase; Pyx = pyroxene; Ox = Fe-Ti oxides.

RESULTS

### Chemical composition and space group of pyroxenes

The chemical compositions of the pyroxenes are presented in Figure 4 and Table 2. Figures 5a and 5b–5e show a high-angle annular dark-field scanning transmission electron microscopy (HAADF-STEM) image and X-ray intensity maps of Al, Fe, Mg, and Ca, respectively, for a pyroxene with a width of ~1 μm in the dense juvenile fragment. This crystal is composed of at least three domains. The bright-field TEM (BF-TEM) image and one of the selected area diffraction (SAD) patterns of each domain taken at a common tilt angle are shown in Figures 5f–5i. The chemical compositions of each domain are presented in Table 2. Based on the chemical compositions and SAD patterns, the phases can be determined as orthopyroxene (*Pbca*; Fig. 5g), Ca-rich augite (*C2/c*; Fig. 5h); and sub-calcic augite (*C2/c*; Fig. 5i). Such a composite pyroxene is not rare in the sample, although statistical counting was not conducted. In Figures 5a–5d, weak concentric compositional zoning was also observed.

A BF-TEM image and SAD patterns of three pyroxene crystals with a diameter of ~20–30 nm in the dense juvenile fragment are shown in Figure 6. The crystals were too small for determining the phase from a diffraction pattern of one particle. Based on the assumption that these pyroxenes have the same structure, the diffraction patterns correspond to the *C2/c* clinopyroxene structure. The zone axes for each diffraction pattern are shown in Figures 6b, 6c, and 6d. The chemical compositions of the pyroxenes ~20–30 nm on a diameter are enriched in iron compared with those for crystals ~1 μm in width, as shown in Figure 4 and Table 2.

Phase identification of Fe-Ti oxide

Figures 7a and 7b show BF-TEM images of a dense juvenile fragment with relatively lower and higher magnifications, respectively. Figure 7c shows a SAD pattern of an Fe-Ti oxide grain ~500 nm in width labeled in Figure 7a, which shows a twin structure and corresponds to the $[1\bar{1}0]$ zone axis of the $Fd\bar{3}m$ structure. Figure 7d shows a Fourier transform image of an Fe-Ti oxide crystal ~10

FIGURE 3. Semi-log crystal size distribution (CSD) plots for pyroxene (upper row) and plagioclase (lower row). The crystal width (shorter side of rectangle) measured in backscattered electron images are used as the crystal size. CSDCorrections (Higgins 2000) was applied to the raw data of Mujin and Nakamura (2014). The used data are crystals from 0.1 to 5.2 μm in width before CSDCorrections is applied. We loaded two separate data sets obtained from scanning electron microscopy with a tungsten filament (W-SEM) and field emission (FE-SEM) to CSDCorrections. The total number of measurements are shown in each panel. (**a** and **b**) Pumices of the sub-Plinian eruptions; (**c** and **d**) pumices of the vulcanian explosions; (**e** and **f**) dense juvenile fragments of the vulcanian explosions.
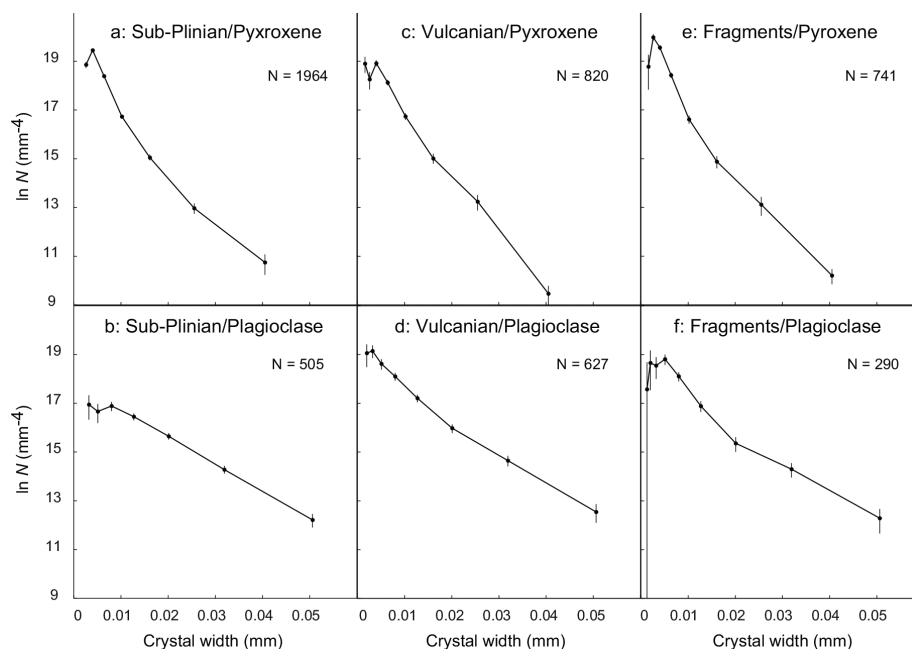
nm on a diameter labeled in Figure 7b, which can be explained by the $Fd\bar{3}m$ structure with zone axis $[0\bar{1}1]$. The proportion of ferric and ferrous iron of the larger ~500 nm crystal was calculated to fit the charge balance assuming that the divalent, trivalent, and tetravalent cations are Mg, Mn, and Fe^{2+}; Al and Fe^{3+}; and Si^{4+} and Ti^{4+}, respectively (Table 3). The X-ray intensity maps of Fe, Ti, Si, Mg, and Ca (Fig. 8) show that the smaller ~10–20 nm crystals contain Ti, although the quantitative value was not obtained owing to the resolution limitation. These crystallographic and chemical data show that the Fe-Ti oxide both ~500 and ~10–20 nm in width are titanomagnetite.

Figures 9a and 9b show a BSE and HAADF-STEM images of a dense juvenile fragment from a vulcanian explosion, respectively. The bright crystals in Figure 9 are titanomagnetite, as determined above. The bright spots in the HAADF-STEM image ~1–2 nm in diameter (Fig. 9b) have most likely Fe-rich compositions judging from their higher brightness in the HAADF-STEM image than that of pyroxene ~20–30 nm on a diameter. Whether these spots are crystalline or amorphous was not identified owing to resolution limitation.

Size ranges and number densities of nanolites and ultrananolites

Redefinition of nanolite and definition of ultrananolite. As shown in Figures 2f and 9, pyroxene and titanomagnetite ~10–30 nm on a diameter and Fe–rich oxide spots <2 nm in diameter are included in the dense juvenile fragment sample. These minute crystals were also observed in parts of the groundmasses of volcanic bombs collected at the Nakadake summit. These crystals have clear size gaps from the larger ones indicating hiatus; pyroxene of ~30–100 nm and Fe-Ti oxide of ~2–10 nm are rare. Therefore, two gaps exist for Fe-Ti oxide; the other gap is from a few hundred nanometers to ~20 nm. In the pumices of sub-Plinian eruptions and vulcanian explosions, crystals smaller than 30 nm were not found in the interstices of microlites and nanolites of pyroxene and plagioclase (Figs. 2b and 2d).

TABLE 1. Parameters for utilizing of CSDCorrections

| Phase | Eruption style | Magni-fication[a] | Crystal shape parameters from CSDSlice | | | | Analyzed area except for vesicles | Roundness | Vesicle | Size scale length |
			x	y	z	R²	(μm²)	(area %)		Number of bins per decade[b]
Pyroxene	Sub-Plinian pumices	high	1.0	1.0	8.0	0.7140	24753	0.4	0.0	5
		low	1.0	2.1	7.0	0.7715	66716			
	Vulcanian pumices	high	1.0	1.2	10.0	0.6533	7026			
		low	1.0	2.1	10.0	0.7315	76836			
	Lithic fragments	high	1.0	1.1	8.0	0.6933	5263			
		low	1.0	2.3	9.0	0.7262	57349			
Plagioclase	Sub-Plinian pumices	high	1.0	5.0	10.0	0.8588	24753	0.2	0.0	5
		low	1.0	4.5	10.0	0.6622	66716			
	Vulcanian pumices	high	1.0	3.4	10.0	0.4933	7026			
		low	1.0	4.0	10.0	0.6993	76836			
	Lithic fragments	high	1.0	4.0	10.0	0.6063	5263			
		low	1.0	5.0	10.0	0.6891	57349			

[a] High and low represent the magnifications of BSE images at which the data were obtained (high = ×5000 with FE-SEM; low = ×1000 with W-SEM). The data used for high and low magnifications are from 0.1 to 5.2 μm and from 0.5 to 5.2 μm, respectively.
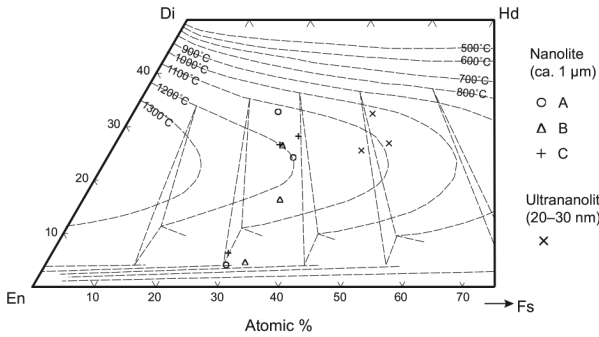[b] Logarithmic base 10 size scale.

FIGURE 4. Chemical compositions of pyroxene in the dense juvenile fragment of the vulcanian explosion. The nanolite crystals (~1 μm) have a composite structure consisting of at least three domains. Each crystal is represented by different symbols (circle, triangle, and cross). The bright-field transmission electron microscopy (BF-TEM) image and the analyzed points of crystal A (circle) are shown in Figure 5. The sizes of ultrananolites analyzed with TEM (x-mark) were ~20–30 nm on a diameter. The polythermal isopleths represent equilibrium pyroxene compositions from Lindsley (1983).

TABLE 3. Chemical composition of magnetite

	Raw	Recalculated[b]
Elements (at%)		
O	56.84	4.00
Si	0.89	0.06
Ti	2.99	0.21
Al	2.39	0.17
Fe^{2+}	35.66	1.18
Fe^{3+}		1.29
Mn	0.19	0.01
Mg	1.04	0.07
Total	100[a]	7.00
Oxides (wt%)		
SiO_2		0.14
TiO_2		0.61
Al_2O_3		0.31
FeO		44.61
Fe_2O_3		54.20
MnO		0.03
MgO		0.11
Total[a]		100.00
X_{usp}		0.25

Notes: The analyzed crystals are shown in Figure 7a.
[a] Recalculated to total 100%.
[b] Recalculated to fit the charge balance.

Mujin and Nakamura (2014) differentiated nanolites from microlites based on the kinks and gaps in the CSD, similar to the first definition of nanolite by Sharp et al. (1996). In this paper, as noted previously, we redefine the term "nanolite" simply as crystals of size 30 nm to 1 μm in width, and "ultrananolite" as those <30 nm in diameter, so that this classification is consistent with those by Cashman (1992) (microlite, 1–30 μm; micropho-

nocryst, 30–100 μm), avoiding the following problems. (1) The crystal sizes at kinks and gaps in CSDs may vary among different minerals, magma compositions, and crystallization processes. This leads to a situation in which minerals in the same size range could be classified into different categories, which is confusing. (2) One may identify nanolites and ultrananolites in their samples without obtaining CSD.

TABLE 2. Chemical compositions of pyroxenes by TEM-EDS analyses

Phase Position	Nanolite (1 μm) A			Nanolite (1 μm) B			Nanolite (1 μm) C			Ultrananolite[f] (20–30 nm)			Glass[g]
	Opx core (x[e])	Aug core (y[e])	Sub-calcic aug rim (z[e])	Opx core	Aug core	Sub-calcic aug rim	Opx core	Aug rim	Aug rim	Ferroaugite			
Elements (at%)[a]													
O	58.87	57.61	57.80	58.95	59.83	59.33	60.74	61.27	63.19				64.19
Si	20.01	20.06	19.51	19.51	18.52	19.10	18.78	18.13	17.71				27.39
Ti	0.06	0.18	0.26	0.14	0.30	0.24	0.10	0.27	0.33				0.21
Al	0.54	1.29	1.43	1.22	1.62	1.38	1.02	1.99	2.16				4.44
Fe	5.94	4.83	6.25	6.42	5.30	6.28	5.46	4.85	4.76				0.48
Mn	0.24	0.22	0.25	0.20	0.24	0.25	0.19	0.22	0.19				
Mg	13.54	9.08	9.50	12.67	9.04	10.22	12.53	8.49	7.06				0.13
Ca	0.80	6.74	4.99	0.89	5.14	3.19	1.18	4.79	4.61				0.27
Na													0.91
K													1.98
Total[b]	100	100	100	100	100	100	100	100	100				100
Wo[c]	3.9	32.6	24.1	4.5	26.4	16.2	6.2	26.4	28.1	25	32	27	26.4
En[c]	66.8	44.0	45.8	63.4	46.4	51.9	65.4	46.8	43.0	34	29	29	46.8
Fs[c]	29.3	23.4	30.1	32.1	27.2	31.9	28.5	26.8	29.0	41	39	44	26.8
Oxides (wt%)[d]													
SiO_2	52.99	50.39	48.94	51.38	49.02	49.96	52.11	49.80	50.69				79.61
TiO_2	0.21	0.60	0.87	0.49	1.06	0.83	0.37	0.99	1.26				0.82
Al_2O_3	1.21	2.75	3.04	2.73	3.64	3.06	2.40	4.64	5.25				10.96
FeO	18.81	14.51	18.75	20.22	16.78	19.65	18.12	15.93	16.29				1.71
MnO	0.75	0.65	0.74	0.62	0.75	0.77	0.62	0.71	0.64				
MgO	24.05	15.30	15.98	22.38	16.05	17.93	23.32	15.64	13.55				0.26
CaO	1.98	15.80	11.68	2.19	12.70	7.79	3.06	12.28	12.32				0.76
Na_2O													1.36
K_2O													4.52
Total[b]	100	100	100	100	100	100	100	100	100				100

[a] The concentration of oxygen was quantified independently.
[b] Recalculated to Total 100%.
[c] Wo = Ca/(Ca+Mg+Fe) atom, En = Mg/(Ca+Mg+Fe) atom, Fs = Fe/(Ca+Mg+Fe) atom.
[d] Weight percentages of the oxides were calculated from the atomic percent of cations.
[e] The analyzed positions of nanolite are shown in Figure 5f.
[f] The solid solution compositions were obtained by subtracting the glass composition from the raw data.
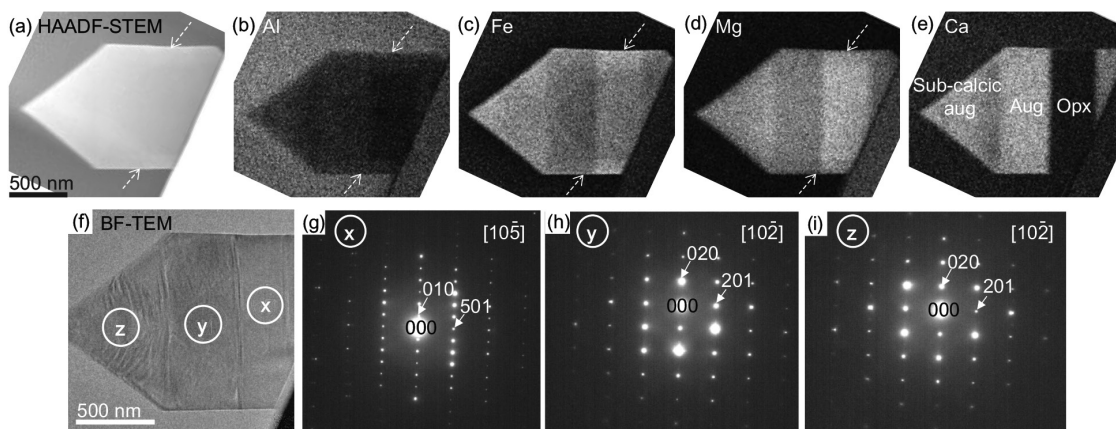[g] The chemical composition of groundmass glass by SEM-EDS spot analyses.

FIGURE 5. (**a**) High-angle annular dark-field scanning transmission electron microscopy (HAADF-STEM) image and (**b–e**) X-ray intensity maps of Al, Fe, Mg, and Ca, respectively, for the same area of a pyroxene nanolite in the dense juvenile fragment. (**g–i**) The selected area diffraction (SAD) patterns obtained from the points x, y, and z in the BF-TEM image (**f**). On the basis of the chemical compositions and SAD patterns, the phases were determined to be orthopyroxene (Opx, *Pbca*) for **g**, Ca-rich augite (Aug, *C2/c*) for **h** and sub-calcic augite (*C2/c*) for **i**, with the electron beam along with [$10\bar{5}$], [$10\bar{2}$], and [$10\bar{2}$] zone axes, respectively. Concentric compositional zoning is observed in **a–d**.
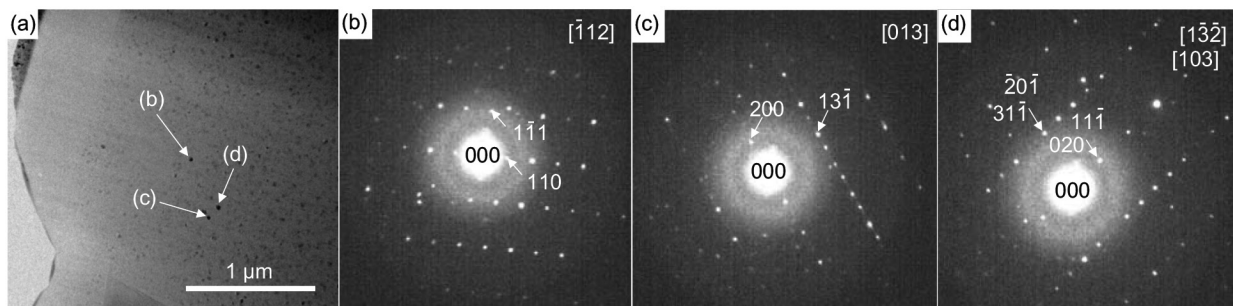
FIGURE 6. (**a**) BF-TEM image of the dense juvenile fragment. (**b–d**) The SAD patterns of pyroxene ultrananolites in **a**. On the assumption that these crystals have the same crystallographic structure, the diffraction patterns correspond to the *C2/c* clinopyroxene structure with the electron beam along the (**b**) [$\bar{1}12$], (**c**) [013], and (**d**) [$1\bar{3}\bar{2}$] or [103] zone axes.

In the FE-SEM (BSE) and TEM (HAADF-STEM) images of Figure 9, some titanomagnetite ultrananolites overlap with pyroxene ultrananolites. Through transmission electron microtomography, however, we can see that most of the titanomagnetite crystals are distributed apart from the pyroxenes. This reveals that the titanomagnetite ultrananolite nucleated homogeneously (Supplemental[1] Material 1).

Figure 10 shows a log-log plot of area number density divided by size intervals (*n**) for pyroxene and Fe-Ti oxide from 1 nm to 5.2 μm in the dense juvenile fragment. The size interval used for the *n** calculation is shown by the length of bars. Dividing by size interval makes it possible to compare the area number densities with different sizes. In Table 4, the appearance and *n** of pyroxene ultrananolite, titanomagnetite microlite and ultrananolite, and Fe-rich spots are summarized with respect to the three groups of erupted products. The raw data of the areal number densities of microlite and ultrananolite of Fe-Ti oxides are the same as those reported by Mujin and Nakamura (2014), although the results were recalculated for this reason. The number of 1–2 nm Fe-rich spots in the HAADF-STEM image (Fig. 9b) was measured for the thin section, throughout its thickness. The raw number density was thus overcounted compared to that counted on the SEM images

of polished surface. We therefore recalculated it by assuming that the section thickness is 100–150 nm.

Minimum crystal size and the smallest measurable number density. In this study, we observed minute spots down to 1 nm by utilizing TEM. The lattice parameters of magnetite and augite are 0.8396 and 0.525–0.98 nm (Deer et al. 1992), respectively; thus, this resolution is fairly close to the theoretically minimum nucleus radius of the minerals. A drawback of such high-magnification observation is a narrowed field of view, which results in high probability of undercounting the crystals. The relation between size and *n** of the observable crystals was calculated as follows and is shown in Figure 10. We obtained BSE images by SEM and HAADF-STEM at magnifications of 50–100 000 and 1 500 000, respectively. At magnifications of 1 500 000, 100 000, 20 000, and 1000, the fields of view were 94 × 100, 1280 × 892, 6400 × 4460, and 1 280 000 × 89 200 nm, and the minimum measurable sizes of the crystals were 1, 5, 25, and 500 nm when that is 5 pixels, respectively. The measurable maximum size was regarded as the shorter (longitudinal) side length of field of view. The size interval to obtain *n** from the area number density should be smaller than this maximum measurable size. The theoretically smallest measurable number density per unit area was obtained by divid-
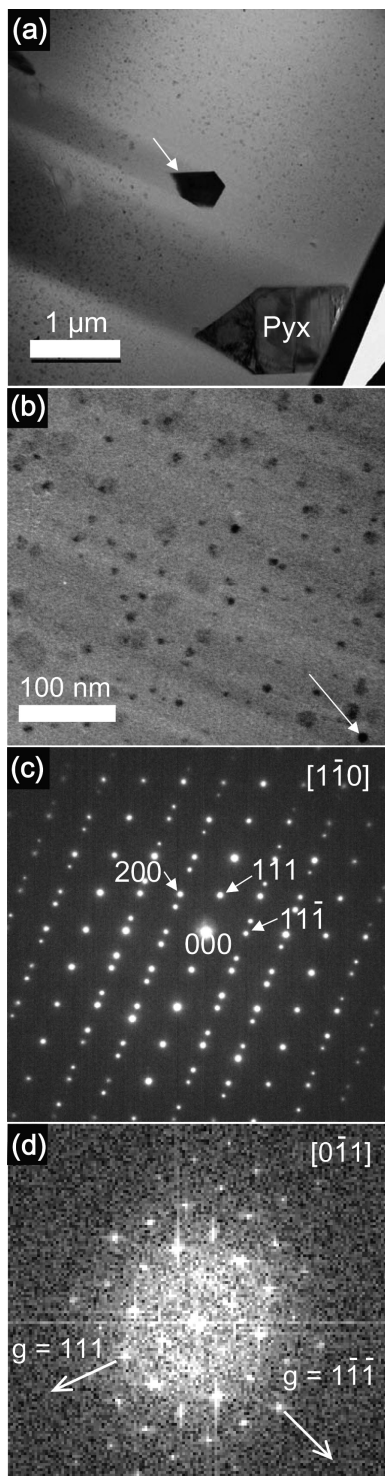
FIGURE 7. (**a** and **b**) BF-TEM images of a dense juvenile fragment with relatively lower and higher magnifications, respectively. Tiny crystals <30 nm on a diameter are absent within ~250–500 nm from the outer rim of pyroxene (Pyx) and titanomagnetite (arrow) with a width of ~0.5–1 μm in **a**. (**c**) SAD pattern of titanomagnetite indicated by the arrow in **a**, showing a twin structure corresponding to the $[1\bar{1}0]$ zone axis of the $Fd\bar{3}m$ structure. (**d**) Fourier transform of a titanomagnetite ultrananolite shown by the arrow in **b**, corresponding to $[0\bar{1}1]$ zone axis of the $Fd\bar{3}m$ structure.

ing the unity by the counted area and then by the maximum size interval, for example at a crystal size of 25 nm (2.5×10^{-5} mm) at magnification of 20000, $n = 1/(6400 \times 4460)/(4460) \approx 7.9^{-12}$ $nm^{-3} = 7.9^6$ mm^{-3}.

Even if this constraint is considered, the gaps or hiatus in the size distribution still exist clearly for pyroxene and titanomagnetite. Another important finding is the presence of minimum crystal sizes except for the Fe-rich spots in the dense fragment. These crystals are ~100 nm for plagioclase in all samples and for pyroxene in the pumices of sub-Plinian and vulcanian eruption, ~20 nm for pyroxene in a dense juvenile fragment, and a few hundred nanometers for Fe-Ti oxide in the pumices of sub-Plinian and vulcanian eruption.

Morphology

Pyroxene microlite and nanolite with a width of 0.1–5.2 μm are generally acicular and often exhibit swallowtail, hopper, and hexagonal shapes in the polished sections. Hollow crystals are also common. These morphological characteristics indicate that the crystals grew rapidly under large undercooling. However, pyroxene ultrananolites on a diameter of 20–30 nm are spherical (Fig. 9 and Supplemental[1] Material 1). The Fe-Ti oxide microlites and nanolite ≥~1 μm generally exhibit a euhedral rectangular shape, whereas ultrananolites (10–20 nm) of Fe-Ti oxide are spherical. It is noteworthy that pyroxene and Fe-Ti oxide ultrananolites are spherical. Two possibilities are considered for the spherical shape. (1) The spherical shape is almost an equilibrium form, resulting from the lack of interfacial free energy anisotropy. It is known that in the case of ionic crystals, equilibrium form is accomplished rather than the growth form when crystal size is equal to or less than one micrometer at high temperatures where atoms move quickly to reduce interfacial energy (Heyraud and Métois 1987). The anisotropy could be weakened either by the effect of thermal fluctuation at high temperature (Herring 1951) or by losing the character of bulk crystal on less than a few nanometer scale crystals (e.g., Buffat and Borel 1976). (2) The spherical shape is a growth form, not dominated by interfacial energy, because of crystal growth at very high undercooling (Welsch et al. 2014).

DISCUSSION

Mineralogical characteristics of pyroxene nanolite and ultrananolite

Contrary to the traditional petrographic view that rapidly grown groundmass pyroxenes are pigeonite, the space group of crystallographically composite pyroxene nanolites are partly sub-calcic augite and augite (C2/c) and orthopyroxene (Pbca) (Fig. 5). The pyroxene ultrananolites are ferroaugite (C2/c). The pyroxene compositions are not plotted on a single isotherm of Lindsley (1983) at 1 atm; instead, they are more or less in disequilibrium (Fig. 4). The augite crystals plot on the 1200 °C, while the Ca-poor pyroxenes in contact with the augite crystals are orthopyroxene, not pigeonite, indicating that the temperature should be lower than ~1100 °C. Under equilibrium, the Ca-poor pyroxene becomes pigeonite at temperatures above 1100 °C. Growth of the sub-calcic augite (C2/c) domain is assumed to have occurred, followed by the crystallization of pyroxene ultrananolite. Sharp et al. (1996) also reported zoned pyroxene nanolites with orthopyroxene cores

FIGURE 8. (a) HAADF-STEM image and (b–f) X-ray intensity maps of Fe, Ti, Si, Mg, and Ca, respectively, in a dense juvenile fragment. The brighter dots in the HAADF-STEM image are titanomagnetite (Ox), which correspond to the brighter dots in the X-ray intensity maps of Fe and Ti. Abbreviation: Pyx = pyroxene.
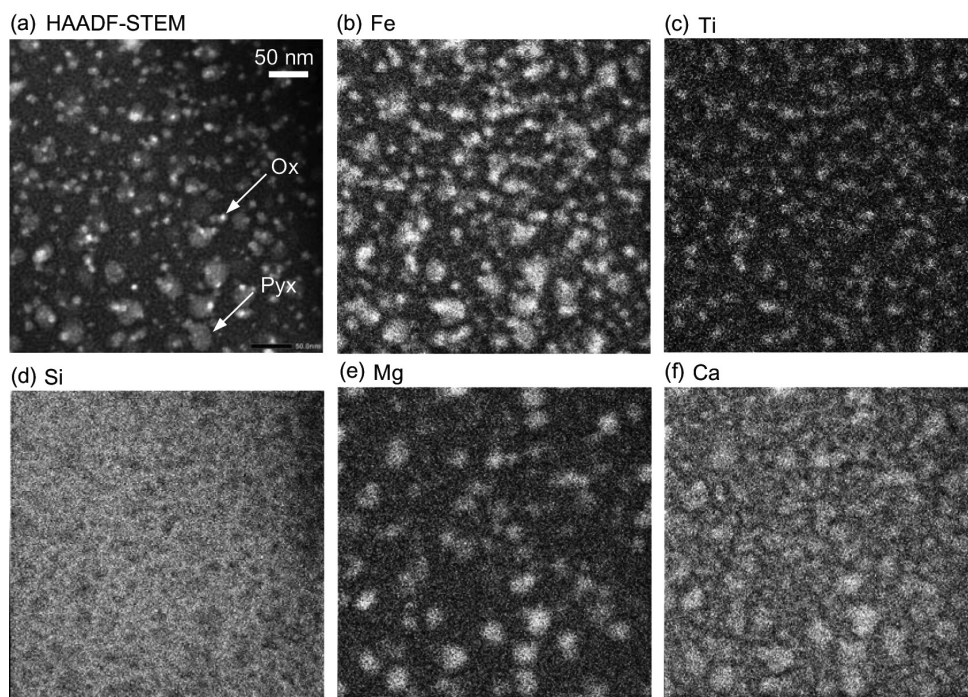
and clinopyroxene rims, though their samples contained pigeonite.

The pyroxene ultrananolites are Fe-rich compared to the sub-calcic augite domain of nanolites by 9–14 mol% in ferrosilite content (Table 2, Fig. 4). This deviation from equilibrium partitioning may be caused by a kinetic effect in rapid growth. The Fe-enrichment of rapidly grown groundmass pyroxene was reported for Apollo 12 lunar basalts by Kushiro et al. (1971).

The pyroxene and titanomagnetite ultrananolites are both absent within ~250–500 nm from the outer rim of pyroxene and magnetite nanolites (Fig. 7a). This shows that the growth rates of the pyroxene and magnetite nanolites were rapid enough to form diffusive boundary layers in which the iron was depleted. Similar compositional boundary layers without ultrananolites were reported for glass-rich andesitic tephra from Southern Taupo Volcanic Zone (Zellmer et al. 2016).

### Crystallization processes of nanolites and ultrananolites

The primary mechanism by which effective undercooling (ΔT) is produced for microlites is assumed to be decompression-

induced dehydration of hydrous magma (Cashman and Blundy 2000). Here, we focus on the crystallization process of nanolites and ultrananolites. Below we examine the production of ΔT based on phase diagrams of simple systems. A primary characteristic of the nanolites and ultrananolites in the present study is their very large number density. A steepening CSD slope of decreasing size was observed through either primitive or high-level stereological corrections for pyroxenes and plagioclase, except for plagioclase in the sub-Plinian pumices. Such an increase in the nucleation rate was possibly caused by an increase of effective ΔT due to progressive degassing, in addition to hindered crystallization differentiation due to decreased diffusivity in the intercrystalline dehydrated melt.

Another major finding is the presence of practical minimum sizes and gap in size distribution. This indicates practical pause (freezing) of nucleation. The kinetics of nucleation and growth are then discussed.

Considerations on phase diagrams. Let us first consider the development of undercooling and crystallization volume with

FIGURE 9. (a) BSE image and (b) HAADF-STEM image of a vulcanian dense juvenile fragment. This fragment, among the five observed fragments includes pyroxene (Pyx) ultrananolites <30 nm on a diameter and Fe-Ti oxide (Ox) ultrananolites <20 nm and Fe-rich spots <2 nm. Abbreviation: UN = ultrananolite.
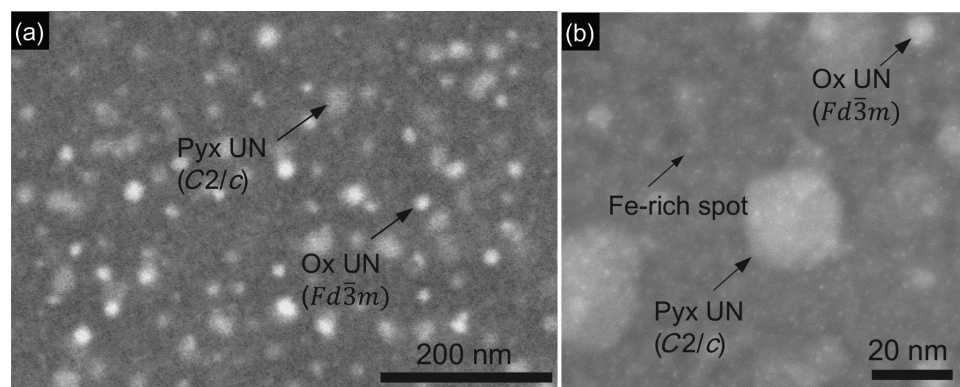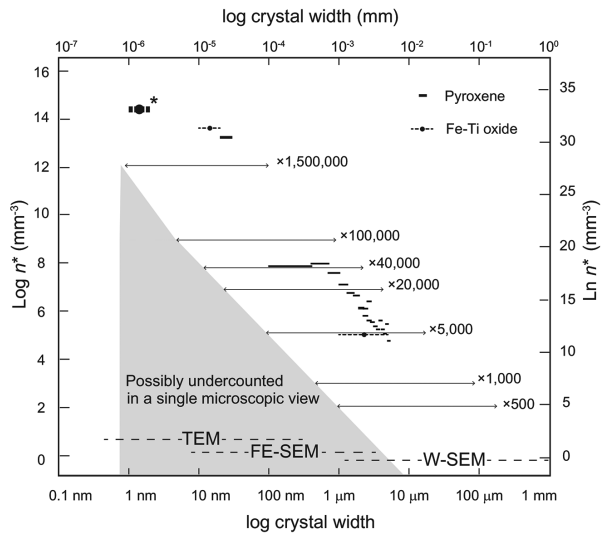
FIGURE 10. Log-log plot of crystal number density per unit area at a given size (width) interval (n^* mm^{-3}) vs. crystal size for pyroxene and Fe-Ti oxide in the dense juvenile fragment. The used data are crystals from 1 nm to 5.2 μm. Data for pyroxene and Fe-Ti oxides are shown by solid and dotted horizontal bars, respectively. Note that crystal size intervals are different for each crystal size, which are shown by the length of the bars (pyroxene: 300 nm interval for <0.1–5.2 μm crystals, 10 nm for 20–30 nm; Fe-Ti oxides: 4 μm for 1–5 μm, 10 nm for 10–20 nm, Fe-rich spots: 1 nm for 1–2 nm). Note that because the Fe-rich spots (*) were observed through the thin sections in HAADF-STEM image, their number density was recalculated into the value of 2D section by assuming the section thickness to be 100–150 nm. The double-arrowed bars represent measurable ranges of crystal size and the lower limit of the crystal number density measureable at the magnification shown. The number density in the shaded area may be undercounted in a single microscopic view at each magnification. The dashed lines at the bottom represent the microscopy applied to the size ranges: TEM, FE-SEM, and W-SEM, respectively.

magma ascent on binary, ternary, and pseudoternary phase diagrams. First, we assumed a system saturated with a single mineral phase (Fig. 11). If crystallization differentiation of the melt catches up with the increase of the liquidus temperature by decompression, ΔT is not produced or does not increase, as shown in the binary phase diagram (Fig. 11). Because the liquidus temperature generally increases more rapidly with decreasing pressure (i.e., approaching the surface), ΔT has the potential to increase rapidly even if the magma decompression rate is constant (e.g., plagioclase: Bowen 1913; Yoder et al. 1957; diopside (Di), anorthite

(An) system: Yoder et al. 1957; Yoder 1965; Weill et al. 1980a).

In multi-component systems, the changes in ΔT for constituting phases may show complex behavior, depending on their relative increase of liquidus temperature with decompression. Here, we consider the Di-An-albite (Ab) system as a representative case. With decreasing water pressure, the liquidus volume of plagioclase expands, and the cotectic boundary shifts toward Di (Fig. 12a). This results in a larger increase in ΔT for the cotectic melt with respect to plagioclase than that for Di, which explains the dominancy of plagioclase as a microlite phase of intermediate magmas. The following plagioclase crystallization results in differentiation of melt and increase in ΔT for Di (Fig. 12b). If the shift of the cotectic composition is significant, the initial cotectic melt could even exceed the metastable liquidus of Di (Fig. 12c). In such a case, crystallization of Di pauses until the melt composition returns to the metastable liquidus by plagioclase crystallization (Fig. 12c).

In the orthpyroxene-plagioclase-SiOr-magnetite (Opx-Pl-SiOr-Mag) pseudoternary system (e.g., Merzbacher and Eggler 1984; Baker and Eggler 1987), the liquidus volume of Pl expands, and the cotectic boundary between Opx and Pl shifts toward Opx with decreasing water pressure. This results in the "liquid line of pressure descent," where the compositional trace of melt is subject to decompression and fractional crystallization, in a direction nearly parallel to the Pl-SiOr line. This indicates that the crystallization volume of plagioclase becomes much larger than that of pyroxenes, which is consistent with the relative amount of ΔT between plagioclase and pyroxenes in the above Di-An-Ab system.

Because nanolite and ultrananolite crystallization may occur at a very low pressure, the effects of cooling and oxidation could also be important, in addition to decompression. The liquidus temperature of Fe-Ti oxides, among others, is strongly affected by oxygen fugacity (e.g., Toplis and Carroll 1995). For example, the liquidus temperature of magnetite increases by 60 °C with increasing f_{O_2} by 2.0 log units from $\Delta QFM = -2.0$ (quartz-fayalite-magnetite) at atmospheric pressure with a ferro-basalt composition.

Factors controlling nucleation rate. Next, we consider the theoretical aspects of crystal nucleation that could have caused the slope change of CSD, occurrence of minimum sizes and gap in the size distribution. Generally, the nucleation rate is controlled by the activation energy of nucleation (ΔG^*), which is proportional to the cube of interfacial energy (σ) between the crystal and melt and inverse to the square of supersaturation ($\Delta \mu$). Dowty (1980) calculated the interfacial energy between alkali feldspar and $NaAlSi_3O_8$-$KAlSi_3O_8$-H_2O melt to be 0.015 J/m^2 at 9.5 wt% H_2O and 0.04 J/m^2 at 1.7 wt% H_2O at a confining pressure of 2.5 kbar. Hammer (2004) obtained the interfacial energy between feldspar and Pinatubo dacite melt based on single-step

TABLE 4. Number density of ultrananolite and microlite in Figure 10

		Sub-Plinian pumice			vulcanian pumice			vulcanian dense juvenile fragment		
		Size range	Size interval	n^{*a} (mm^{-3})	Size range	Size interval	n^{*a} (mm^{-3})	Size range	Size interval	n^{*a} (mm^{-3})
Pyroxene	ultrananolite	–			–			20–30 nm	10 nm	1.7×10^{13}
Fe-Ti oxide	microlite	1–5 μm	4 μm	5.7×10^4	1–8 μm	7 μm	1.2×10^7	1–5 μm	4 μm	1.0×10^5
	ultrananolite	–			–			10–20 nm	10 nm	4.1×10^{13}
Fe-rich spot[b]	ultrananolite	–			–			1–2 nm	1 nm	$1.9–2.9 \times 10^{14}$

Notes: Microlite and ultrananolite of Fe-Ti oxide of the vulcanian dense juvenile fragment were recalculated from the results of Mujin and Nakamura (2014). No plagioclase ultrananolite was observed in any erupted materials.
[a] The crystal number densities (n^*) were number of crystals at a size interval per unit area (mm^{-3}).
[b] The number of Fe-rich spots in the HAADF-STEM image was measured for all through the thin section. The raw number density was thus overcounted compared to that counted on the SEM images of polished surface. We therefore recalculated it by assuming that the section thickness is 100–150 nm.
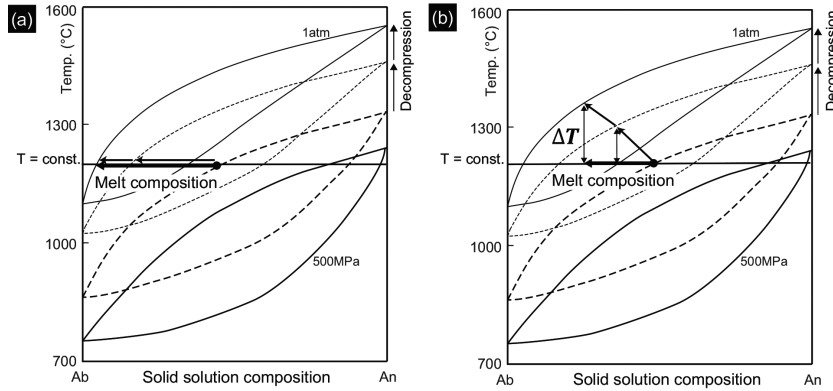
FIGURE 11. Schematic illustrations of the development of undercooling (ΔT) and evolution of melt composition with decompression of volatile-saturated magma on a binary phase diagram of plagioclase. The solidus lines are from Johannes (1978; 500 MPa, H_2O saturated) and Bowen (1913; 1 atm, dry). The liquidus lines are from Yoder et al. (1957; 500 MPa, H_2O saturated) and Bowen (1913; 1 atm, dry). We complemented the solidus and liquidus lines except for 500 MPa and 1 atm. (**a**) If crystallization differentiation of melt catches up with the increase in the liquidus temperature by decompression, ΔT is kept constant. (**b**) If the liquidus temperature increase accelerates with decreasing pressure (i.e., approaching the surface), ΔT may further increase. Note that the illustrated temperature does not correspond to that of Shinmoedake magma.
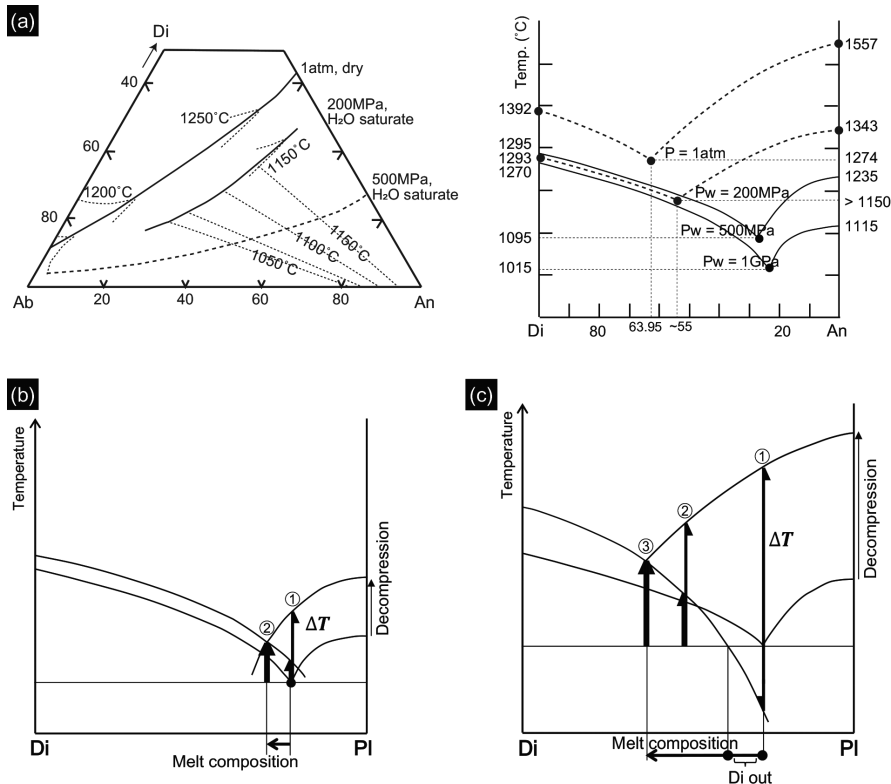

FIGURE 12. (**a**) Schematic illustrations of the development of undercooling (ΔT) and evolution of melt composition with magma decompression in the diopside (Di)–anorthite (An)–albite (Ab) ternary phase diagram. The cotectic lines are from Weill et al. (1980b; 1 atm, dry), Nakamura and Shimakita (1998; 200 MPa, H_2O saturated), and Yoder (1965; 500 MPa, H_2O saturated). The An liquidus temperatures are from Weill et al. (1980a; 1 bar, dry), Yoder et al. (1957; 200 MPa, H_2O saturated), and Yoder (1965; 500 MPa and 1 GPa, H_2O saturated). The Di liquidus temperatures are from Ziegler and Navrotsky (1986; 1 bar, dry), Eggler and Burnham (1984; 200 MPa, H_2O saturated), Yoder (1965; 500 MPa, H_2O saturated), and Perchuk et al. (1988; 1 GPa, H_2O saturated). The Di-An eutectic point at 1 GPa is from Yoder (1965). (**b**) With decreasing water pressure, the liquidus volume of the plagioclase expands, and the cotectic composition shifts toward Di. This results in a larger increase in ΔT for the initial cotectic melt with respect to plagioclase than that with respect to Di. The following plagioclase crystallization causes differentiation of melt and increased ΔT for Di. (**c**) If decompression and the resulting shift in the cotectic composition are significant, the initial cotectic melt may be above the metastable liquidus of Di. In such a case, the crystallization of Di is suspended until the melt composition returns to the metastable liquidus through plagioclase crystallization.
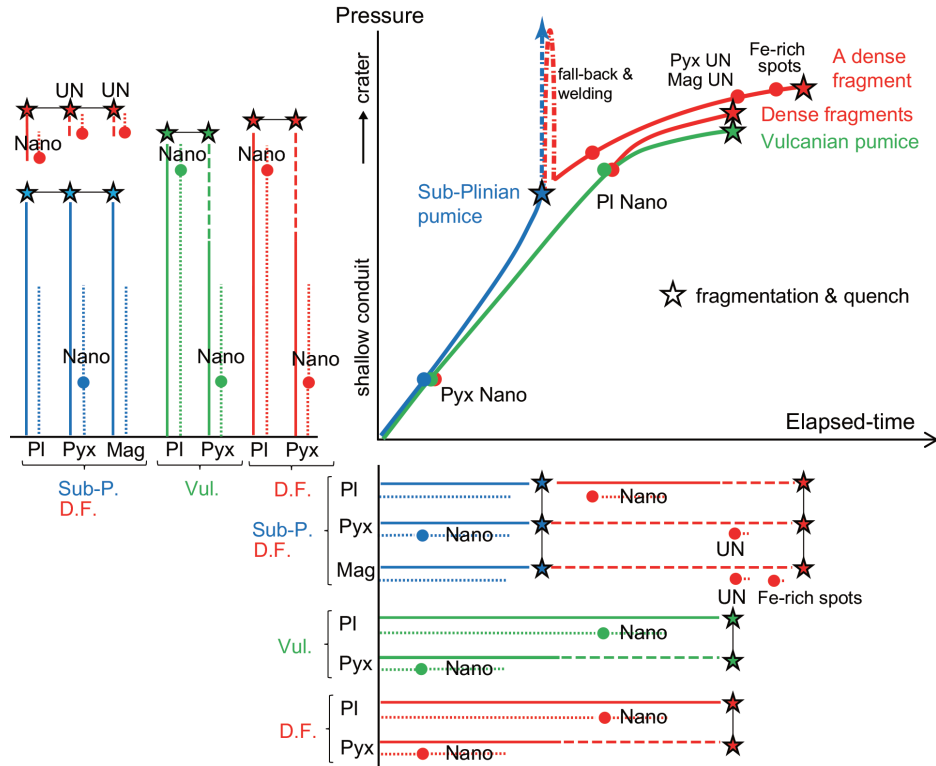
FIGURE 13. Schematic illustration of crystallization sequences and timings of groundmass crystals and their relationship with magma ascent and fragmentation during the Shinmoedake 2011 eruption. The pressure–time path and timing of the fragmentation of the magmas that caused the sub-Plinian eruption are shown in blue; those for the vulcanian eruption are shown in green. Two origins are assumed for the dense juvenile fragments from the vulcanian explosions (red). Some pumice clasts likely fell from the sub-Plinian eruption column back into the crater and were welded at relatively oxidized conditions to form ultrananolites of pyroxene and Fe-Ti oxides. The other type of dense fragment, which is free of ultrananolites, is assumed to have been part of extrusion lava. The dotted and solid bars at the bottom and left parts of the diagram represent durations of nucleation and growth of the crystals, respectively. The dashed part represents the period in which the growth was so small that the CSDs practically did not change. The transit time of the vulcanian magmas in the shallow conduit was longer than that of the sub-Plinian magma. The nucleation practically paused (froze) to some degree before the magma quenching for all minerals in all styles of eruption except for the Fe-rich spots. Compared with plagioclase, the increase of nucleation rate for pyroxene was formed earlier, and the nucleation of pyroxene practically paused (froze) earlier. Abbreviations: Pyx = pyroxene; Pl = plagioclase; Mag = magnetite; UN = ultrananolite; Nano = increase of nucleation rate of nanolite.

decompression experiments and the nucleation theory. The values increased systematically from 0.024 to 0.100 J/m² with a decrease in H_2O content from 4.8 to 0.8 wt%. Assuming nearly constant temperature, the interfacial energy may increase significantly in the intermediate-silicic melt under very low pressure.

The nucleation rate depends also on the melt diffusivity (e.g., Toramaru 1991). Hammer and Rutherford (2002) showed in their single-step decompression crystallization experiments of dacitic melt that the nucleation rates of plagioclase dropped at very high effective ΔT, forming a bell-shaped nucleation rate against ΔT. They attributed the decrease in the nucleation rate to increased melt viscosity and decreased mobility of plagioclase-forming components owing to dehydration.

Origins of ultrananolite, minimum crystal size, and gap in size distribution. In the "transient nucleation" processes, the critical nucleation size is defined as a size above which the number of growing "subcritical clusters," either crystalline or amorphous, exceeds that of decaying ones (e.g., Kelton 1995). The ultrananolite-sized particles observed in the quenched lithic

fragment could be either stable crystals or subcritical clusters. The minimum crystal size may occur when groundmass crystallization enters the growth stage, i.e., when nucleation pauses (freezes) while growth continues. At this stage, the subcritical clusters should decay or be consumed (eaten) by the growing stable nuclei and become eventually unobservable. This is expected to occur when the critical nucleation size increases and the number flux of growing subcritical clusters decreases through a decrease of $\Delta \mu$ (ΔT), increase of σ, and decrease of diffusivity in the melt.

On the other hand, the gap in size distribution is assumed to have been formed when the decaying subcritical clusters are left quenched, or nucleation was resumed after the subcritical clusters had disappeared. Two gaps in the size distribution of Fe-Ti oxide cannot be explained by a single nucleation process; in this case, resumption of nucleation was required.

Kuo and Kirkpatrick (1982) reported that the critical nuclei radius of diopside from the undercooled melt having a similar composition was determined with small angle X-ray scattering (SAXS) to be 35–70 nm, when the undercooling (ΔT) was

10–20 °C. We assume that the undercooling should have been larger in the samples in this study, as shown in Figure 12a, and thus critical radius was smaller. Considering the lattice constant of pyroxenes, we expect the critical nucleation radius to be larger than a few nanometers. The ultrananolite-sized particle might, therefore, include subcritical clusters.

ΔT change during eruption. In volcanic eruptions, an accelerated increase in ΔT may be caused by magma ascent and degassing in shallow conduits owing to the nearly parabolic pressure dependence of water solubility in the melt, as discussed in detail by Mollo and Hammer (2017). This explains the crystallization of high number density nanolites. Thereafter, the ΔT may decrease with the progress of nanolite crystallization. Together with an increase in σ and a decrease of diffusivity, decrease of ΔT contributes to form minimum size. A situation that may produce large ΔT and enable following resumption of ultrananolite crystallization includes rewelding of magma spatters near the craters, i.e., formation of agglutinates (Sumner et al. 2005), clastogenic (or rootless) lavas (e.g., Yasui and Koyaguchi 2004), and tuffisites (Castro et al. 2014). In these rocks, rapid decompression is followed by extensive dehydration and possibly oxidation by fragmentation, whereas high temperature was maintained in the interiors of the magma fragments.

IMPLICATIONS

The notable results obtained from our analyses are as follows. (1) The CSD slope of plagioclase in sub-Plinian pumices did not increase with decreasing size, whereas those in the vulcanian pumices and dense juvenile fragments increased (Fig. 3). (2) In contrast, the CSD slopes of pyroxene in all the erupted materials increased with decreasing size. The CSDs did not change from sub-Plinian to vulcanian pumices (Fig. 3). (3) The minimum crystal sizes were observed for all the minerals except for the Fe-rich spots. The gaps in the size distribution were found for pyroxene and Fe-Ti oxides in the size range of less than ~100 nm (Fig. 10). The observations in 1 and 2 indicated that the timing of the increase of nucleation rate was earlier for pyroxene than for plagioclase, and that the nucleation and growth of pyroxene is completed mostly before the increase of nucleation rate of plagioclase. This is consistent with observation 3, that the nucleation of pyroxene in the sub-Plinian pumice paused before eruption, resulting in the presence of minimum-sized crystals.

The shallow magmatic processes of the 2011 Shinmoedake eruption can be constrained from the above observations on groundmass crystallization as follows (Fig. 13). Observations 1 and 2 clearly imply that until the stage of pyroxene nanolite crystallization, the magma ascent rates were so similar as to be indistinguishable by crystallization between the sub-Plinian and lava extrusion-vulcanian phases, and that magma fragmentation of the sub-Plinian eruption occurred before the increase of nucleation rate for plagioclase. Observation 3 suggests that some lithic fragments have a clastogenic origin. After welding, the magma continuously dehydrated, and plagioclase nucleation rate may have increased, leading to the resumption of pyroxene and Fe-Ti oxide ultrananolite crystallization. In the lava extrusion-vulcanian phase, magma fragmentation occurred after the increase of nucleation rate for plagioclase. The emplacement processes of the non-clastogenic effusive lava and magma erupted as vulcanian pumice were so

similar as to be indistinguishable from the groundmass crystallization. By experimentally determining the crystallization conditions of (ultra)nanolites, such as pressure, temperature, duration, and f_{O_2}, the depth and timing that controlled the eruption style transition can be constrained.

REFERENCES CITED

Baker, D.R., and Eggler, D.H. (1987) Compositions of anhydrous and hydrous melts coexisting with plagioclase, augite, and olivine or low-Ca pyroxene from 1 atm to 8 kbar; application to the Aleutian volcanic center of Atka. American Mineralogist, 72, 12–28.

Bowen, N.L. (1913) The melting phenomena of the plagioclase feldspars. American Journal of Science, 210, 577–599.

Buffat, P., and Borel, J.P. (1976) Size effect on the melting temperature of gold particles. Physical Review A, 13, 2287–2298.

Cashman, K.V. (1992) Groundmass crystallization of Mount St. Helens dacite, 1980–1986: a tool for interpreting shallow magmatic processes. Contributions to Mineralogy and Petrology, 109, 431–449.

Cashman, K.V., and Blundy, J. (2000) Degassing and crystallization of ascending andesite and dacite. Philosophical Transactions of the Royal Society of London A: Mathematical, Physical and Engineering Sciences, 358, 1487–1513.

Castro, J.M., Cashman, K.V., and Manga, M. (2003) A technique for mesuaring 3D crystal-size distributions of prismatic microlites in obsidian, American Mineralogist, 88, 1230–1240.

Castro, J.M., Bindeman, I.N., Tuffen, H., and Schipper, C.I. (2014) Explosive origin of silicic lava: textural and δD–H2O evidence for pyroclastic degassing during rhyolite effusion. Earth and Planetary Science Letters, 405, 52–61.

Deer, W.A., Howie, R.A., and Zussman, J. (1992) An Introduction to the Rock-Forming Minerals, 2nd ed., p. 177 and 558. Prentice Hall.

Dowty, E. (1980) Crystal growth and nucleation theory and the numerical simulation of igneous crystallization. In R.B. Hargraves, Ed., Physics of Magmatic Processes, 419–485. Princeton University Press, New Jersey.

Eggler, D.H., and Burnham, C.W. (1984) Solution of H2O in diopside melts: A thermodynamic model. Contributions to Mineralogy and Petrology, 85, 58–66.

GeomapNavi (2016) The national institute of advanced industrial science and technology (AIST), Geological map display system. Geological Survey of Japan, https://gbank.gsj.jp/geonavi/?lang=en (accessed October 2016).

Geospatial Information Authority of Japan (GSI) (2014) GSI Maps, http://maps.gsi.go.jp/ (accessed April 2014).

Hammer, J.E. (2004) Crystal nucleation in hydrous rhyolite: Experimental data applied to classical theory. American Mineralogist, 89, 1673–1679.

Hammer, J.E., and Rutherford, M.J. (2002) An experimental study of the kinetics of decompression-induced crystallization in silicic melt. Journal of Geophysical Research, 197, 1–23.

Herring, C. (1951) Some theorems on the free energies of crystal surfaces. Physical Review, 82, 87–93.

Heyraud, J.C., and Métois, J.J. (1987) Equilibrium shape of an ionic crystal in equilibrium with its vapour (NaCl). Journal of Crystal Growth, 84, 503–508.

Higgins, M.D. (2000) Measurement of crystal size distributions. American Mineralogist, 85, 1105–1116.

Japan Coast Guard (JCG) (2014) Hydrographic and Oceanographic Department, http://www1.kaiho.mlit.go.jp/jishin/sokuryo/sokuryo.html (accessed April 2014).

Japan Meteorological Agency (JMA) (2011) Volcanic Activity Documents of Kirishimayama volcano, http://www.data.jma.go.jp/svd/vois/data/tokyo/STOCK/monthly_v-act_doc/monthly_vact_505.html (accessed December 1, 2016) (in Japanese).

Japan Meteorological Agency (JMA) (2012) Volcanic activity of Kirishimayama Volcano, February, 2011–May 2011. Report of Coordinating Committee for Prediction of Volcanic Eruption, 109, 139–167 (in Japanese).

Japan Meteorological Agency (JMA) (2016) National Catalogue of the Active Volcanoes in Japan (The fourth edition, English version), http://www.data.jma.go.jp/svd/vois/data/tokyo/STOCK/souran_eng/menu.htm (accessed October 8, 2016).

Johannes, W. (1978) Melting of plagioclase in the system Ab-An-H2O and Qz-Ab-An-H2O at P_{H_2O} = 5 kbars, an equilibrium problem. Contributions to Mineralogy and Petrology, 66, 295–303.

Johannsen, A. (1931) A Descriptive Petrography of the Igneous Rocks, 1, 37. The

University of Chicago Press, Illinois.

Kamada, T. (2014) MapMap ver.6.0, A blank map, http://www5b.biglobe.ne.jp/t-kamada/CBuilder/mapmap.htm (accessed April 2014).

Kelton, K.F. (1995) Transient nucleation in glasses. Materials Science and Engineering: B, 32, 145–152.

Kozono, T., Ueda, H., Ozawa, T., Koyaguchi, T., Fujita, E., Tomiya, A., and Suzuki, Y.J. (2013) Magma discharge variations during the 2011 eruptions of Shinmoedake volcano, Japan, revealed by geodetic and satellite observations. Bulletin of Volcanology, 75, 695–707.

Kuo, L.C., and Kirkpatrick, R.J. (1982) Small angle X-ray scattering study of pre-nucleation behavior of titanium-free and titanium-bearing diopside glasses. American Mineralogist, 67, 676–685.

Kushiro, I., Nakamura, Y., Kitayama, K., and Akimoto, S. (1971) Petrology of some Apollo 12 crystalline rocks. Proceedings of the Second Lunar Science Conference, 1, 481–495.

Lindsley, D.H. (1983) Pyroxene thermometry. American Mineralogist, 68, 477–493.

Merzbacher, C., and Eggler, D.H. (1984) A magmatic geohygrometer: application to Mount St. Helens and other dacitic magmas. Geology, 12, 587–590.

Miyabuchi, Y., Hanada, D., Niimi, H., and Kobayashi, T. (2013) Stratigraphy, grain-size and component characteristics of the 2011 Shinmoedake eruption deposits, Kirishima Volcano, Japan. Journal of Volcanology and Geothermal Research, 258, 31–46.

Mollo, S., and Hammer, J.E. (2017) Dynamic crystallization in magmas. EMU Notes in Mineralogy, 16, 373–418.

Morgan, D.J., and Jerram, D.A. (2006) On estimating crystal shape for crystal size distribution analysis. Journal of Volcanology and Geothermal Research, 154, 1–7.

Mujin, M., and Nakamura, M. (2014) A nanolite record of eruption style transion. Geology, 42, 661–614.

Nakada, S., Nagai, M., Kaneko, T., Suzuki, Y., and Maeno, F. (2013) The outline of the 2011 eruption at Shinmoe-dake (Kirishima), Japan. Earth, Planets and Space, 65, 475–488.

Nakamura, M., and Shimakita, S. (1998) Dissolution origin and syn-entrapment compositional change of melt inclusion in plagioclase. Earth and Planetary Science Letters, 161, 119–133.

Ozawa, T., and Kozono, T. (2013) Temporal variation of the Shinmoe-dake crater in the 2011 eruption revealed by spaceborne SAR observations. Earth, Planets and Space, 65, 527–537.

Paulick, H., and Franz, G. (1997) The color of pumice: case study on a trachytic fall deposit, Meidob volcanic field, Sudan. Bulletin of Volcanology, 59, 171–185.

Perchuk, L.L., Kushiro, I., and Kosyakov, A.V. (1988) Exprimental determination of the liquidus surface in the system diopside-water. Geokhimiya, 7, 942–955 [not seen; extracted from Perchuk, L.L., and Kushiro, I. (1991) Thermodynamics of the Liquidus in the System Diopside–Water: A Review. In L.L. Perchuk and I. Kushiro, Eds., Physical Chemistry of Magmas, 249–267. Springer-Verlag, New York].

Reed, W.P. (1993) Certificate of analysis for standard reference material 2063a. National Institute of Standards and Technology, Gaithersburg, Maryland.

Schlinger, C.M., Smith, R.M., and Veblen, D.R. (1986) Geologic origin of magnetic volcanic glasses in the KBS tuff. Geology, 14, 959–962.

Schlinger, C.M., Rosenbaum, J.G., and Veblen, D.R. (1988) Fe-oxide microcrystals in welded tuff from southern Nevada: Origin of remanence carriers by precipitation in volcanic glass. Geology, 16, 556–519.

Sharp, T.G., Stevenson, R.J., and Dingwell, D.B. (1996) Microlites and "nanolites" in rhyolitic glass: microstructural and chemical characterization. Bulletin of Volcanology, 57, 631–640.

Shimbori, T., Sakurai, T., Tahara, M., and Fukui, K. (2013) Observation of eruption clouds with weather radars and meteorological satellite: a case study of the eruption at Shinmoedake volcano in 2011. Quarterly Journal of Seismology, 77, 139–214.

Sumner, J.M., Blake, S., Matela, R.J. and Wolff, J.A. (2005) Spatter. Journal of Volcanology and Geothermal Research, 142, 49–65.

Suzuki, Y., Yasuda, A., Hokanishi, N., Kaneko, T., Nakada, S., and Fujii, T. (2013) Syneruptive deep magma transfer and shallow magma remobilization during the 2011 eruption of Shinmoe-dake, Japan—Constraints from melt inclusions and phase equilibria experiments. Journal of Volcanology and Geothermal Research, 257, 184–204.

Toramaru, A. (1991) Model of nucleation and growth of crystals in cooling magmas. Contributions to Mineralogy and Petrology, 108, 106–117.

Toplis, M.J., and Carroll, M.R. (1995) An experimental study of the influence of oxygen fugacity on Fe-Ti oxide stability, phase relations, and mineral-melt equilibria in ferro-basaltic systems. Journal of Petrology, 36, 1137–1170.

Watanabe, M., and Williams, D.B. (2006) The quantitative analysis of thin specimens: a review of progress from the Cliff-Lorimer to the new ξ-factor methods. Journal of Microscopy, 221, 89–109.

Weill, D.F., Stebbins, J.F., Hon, R., and Carmichael, I.S.E. (1980a) The enthalpy of fusion of anorthite. Contributions to Mineralogy and Petrology, 74, 95–102.

Weill, D.F., Hon, R., and Navrotsky, A. (1980b) The igneous system $CaMgSi_2O_6$-$CaAl_2Si_2O_8$-$NaAlSi_3O_8$: variations on a classic theme by Bowen. In R.B. Hargraves, Ed., Physics of Magmatic Processes, 49–92. Princeton University Press, New Jersey.

Welsch, B., Hammer, J., and Hellebrand, E. (2014) Phosphorus zoning reveals dendritic architecture of olivine. Geology, 42, 867–870.

Yasui, M., and Koyaguchi, T. (2004) Sequence and eruptive style of the 1783 eruption of Asama Volcano, central Japan: a case study of an andesitic explosive eruption generating fountain-fed lava flow, pumice fall, scoria flow and forming a cone. Bulletin of Volcanology, 66, 243–262.

Yoder, H.S. (1965) Diopside-anorthite-water at five and ten kilobars and its bearing on explosive volcanism. Carnegie Institution of Washington Yearbook, 64, 82–89.

Yoder, H.S., Stewart, D.B., and Smith, J.R. (1957) Ternary feldspars. Carnegie Institution of Washington Yearbook, 56, 206–214.

Zellmer, G.F., Sakamoto, N., Hwang, S.L., Matsuda, N., Iizuka, Y., Moebis, A., and Yurimoto, H. (2016) Inferring the effects of compositional boundary layers on crystal nucleation, growth textures, and mineral chemistry in natural volcanic tephras through submicron-resolution imaging. Frontiers in Earth Science, 4, 88.

Ziegler, D., and Navrotsky, A. (1986) Direct measurement of the enthalpy of fusion of diopside. Geochimica et Cosmochimica Acta, 50, 2461–2466.

Endnote:

[1]Deposit item AM-17-126052, Supplemental Material. Deposit items are free to all readers and found on the MSA web site, via the specific issue's Table of Contents (go to http://www.minsocam.org/MSA/AmMin/TOC/2017/Dec2017_data/Dec2017_data.html).